New two-dimensional phase of tin chalcogenides: Candidates for high-performance thermoelectric materials

Baojuan Dong,[1,2,3] Zhenhai Wang,[3,4,*] Nguyen T. Hung,[5] Artem R. Oganov,[3,6,7] Teng Yang,[1,2,†] Riichiro Saito,[5] and Zhidong Zhang[1,2]

[1]*Shenyang National Laboratory for Materials Science, Institute of Metal Research, Chinese Academy of Sciences, Shenyang 110016, China*

[2]*University of Chinese Academy of Sciences, Beijing 100049, China*

[3]*Skolkovo Institute of Science and Technology, Skolkovo Innovation Center, 3 Nobel St., Moscow 143026, Russia*

[4]*School of Telecommunication and Information Engineering, Nanjing University of Posts and Telecommunications, Nanjing, Jiangsu 210003, China*

[5]*Department of Physics, Tohoku University, Sendai 980-8578, Japan*

[6]*Moscow Institute of Physics and Technology, 9 Institutskiy Lane,Dolgoprudny City, Moscow Region 141700, Russia Federation*

[7]*International Center for Materials Discovery, Northwestern Polytechnical University, Xi'an 710072, People's Republic of China*

(Received 22 October 2018; revised manuscript received 8 December 2018; published 11 January 2019)

Tin-chalcogenides SnX (X = Te, Se, and S) have been attracting research interest due to their thermoelectric physical properties. Their two-dimensional (2D) counterparts, which are expected to enhance those properties, nevertheless have not been fully explored because of many possible structures. A variable-composition exploration of 2D $Sn_{1-x}X_x$ systems (X = Te, Se, and S) has been performed using a global searching method based on an evolutionary algorithm combined with density-functional calculations. A new hexagonal phase denoted by β'-SnX is found using Universal Structure Predictor: Evolutionary Xtallography (USPEX), and the structural stability has been further checked by calculations of phonons and elasticity. β'-SnTe is the most stable among all possible 2D phases of SnTe, including experimentally available phases. Further, β' phases of SnSe and SnS are also found to be energetically close to the most stable phases. A high thermoelectronic (TE) performance has been predicted in the β'-SnX phases, which have a dimensionless figure of merit as high as ∼0.96 to 3.81 for SnTe, ∼0.93 to 2.51 for SnSe, and ∼1.19 to 3.18 for SnS at temperatures ranging from 300 to 900 K with a practically attainable carrier concentration of 5×10^{12} cm^{-2}. The high TE performance results from a high power factor that is attributed to the quantum confinement of 2D materials and the band convergence near the Fermi level, as well as low thermal conductivity mainly from both low elastic constants due to weak inter-Sn bonding strength and strong lattice anharmonicity.

DOI: 10.1103/PhysRevMaterials.3.013405

I. INTRODUCTION

Group IV-VI alloys and their many physical properties have been studied intensively. These properties include ferroelectricity [1], topological insulators [2], and, in particular, thermoelectricity [3–5]. Thermoelectric (TE) materials, which directly convert waste heat into electricity, have attracted increasing attention in the past few decades. The conversion efficiency of TE materials can be evaluated by the dimensionless figure of merit ZT ($= \frac{\sigma S^2}{\kappa}T$, where σ, S, κ, and T represent the electrical conductivity, the Seebeck coefficient, thermal conductivity, and temperature, respectively). Among the group IV-VI alloys, tin and lead chalcogenides [3–6] have been attracting increasing interest in the thermoelectric community due to their electronic structural anisotropy and intrinsic lattice anharmonicity [5,6]. Lattice anharmonicity helps to suppress thermal conductivity, while anisotropy is related to the confinement effect, which has proven to be efficient in improving thermoelectric performance according to Hicks-Dresselhaus theory [7,8] if the confinement length is smaller than the thermal de Broglie length [9].

With the development of the exfoliation and synthesis methods, many two-dimensional (2D) van der Waals materials, including graphene, black phosphorene (BP), transition-metal dichalcogenides (TMDs), and tin chalcogenide (SnX), have been synthesized [10–13]. The exfoliated semiconducting monolayer BP and SnX have demonstrated a much improved thermoelectric performance ($ZT \sim 2.5$ [14] and 2.63 [15] at 500 and 700 K, respectively) with respect to their bulk counterparts. Therefore, it is reasonable to focus our attention on 2D tin chalcogenides, which are promising candidates for high-performance TE materials. So far, other than some limited theoretical calculations [15,16], there have only been a few studies of TE properties of 2D tin chalcogenides. Moreover, 2D forms may exhibit many different structures compared with the bulk counterpart, especially for nonlayered bulks [17,18]. Thus, there is an understandable interest in investigating theoretically the most stable structure among all the possible forms, and to explore the potential TE performance.

In this work, using the Universal Structure Predictor: Evolutionary Xtallography (USPEX) method [19–22], we survey

*physicswzh@gmail.com
†yangteng@imr.ac.cn

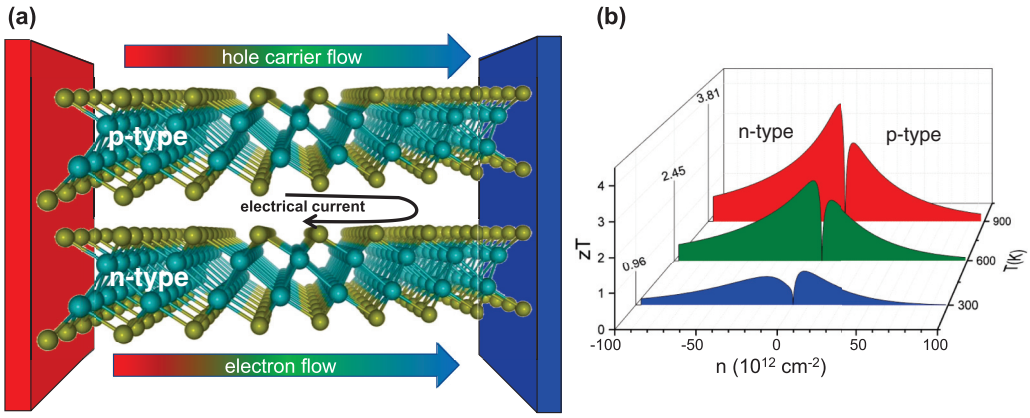

FIG. 1. Promising thermoelectric properties of the new structural phase of SnTe. (a) Schematics of β'-SnTe for thermoelectrics, and (b) temperature- and carrier-concentration-dependent dimensionless figure of merit ZT. The values (0.96, 2.45, and 3.81) on the left panel are the peak ZT values of β'-SnTe at 300, 600, and 900 K, respectively.

all possible tin-chalcogenide 2D phases. A new hexagonal SnX (X = Te, Se, and S) phase, which is called the β' phase and is shown in Fig. 1(a), has been found by using USPEX. The β'-SnX have been found to be thermodynamically stable. Due to the low lattice thermal conductivity κ_l and high σ, as explained in the following section, high thermoelectric performance is achieved in the β'-SnX phases. For example, as seen in Fig. 1(b), ZT of β'-SnTe at a carrier concentration of around a few 10^{12} cm^{-2} can be up to 2.45 and 3.81 at 600 and 900 K, respectively.

The paper is organized as follows. We briefly introduce the computational methods in Sec. II. In Sec. III we shows the main results of β'-SnX, including structural stability in Sec. IIIA, thermal transport properties in Sec. IIIB, and thermoelectric properties in Sec. IIIC. Finally, we draw conclusions in Sec. IV.

II. METHOD

The structure search of 2D tin chalcogenides is performed by USPEX [19–22] combined with the Vienna *ab initio* simulation package (VASP) [23]. In our variable-composition USPEX calculations, the thickness of 2D crystals is restricted in a range of 0–6 Å, the total number of atoms is set to be 2–12. The initial population of structures was produced by random symmetric structure generator using 80 layer groups of symmetry; this population then evolved, driven by natural selection and action of variation operators (crossover and mutations). Total energy is calculated within the framework of the projector-augmented wave (PAW) method [24]. The generalized gradient approximation (GGA) [25] is used for treating the electronic exchange-correlation interaction. More details on the parameters can be found in the Supplemental Material [26].

Electronic transport properties are calculated by solving the semiclassical Boltzmann transport equation within the constant relaxation time approximation as implemented in the BoltzTraP package [27]. Since there are no experimental data on the electrical conductivity available for the new β'-phases to evaluate the relaxation time τ, τ is estimated based on carrier mobility μ, for example $\tau = \frac{m^*\mu}{e}$, m^* is the effective mass of the carrier, and carrier mobility μ is calculated based on the deformation potential theory [28–33]. The calculated τ at room temperature varies from a few tens to a few hundred femtoseconds (10^{-15} s), which has the same order of magnitude as the calculated values in other 2D materials [34,35]. More details on how to get the carrier mobility μ and relaxation time τ can be found in the Supplemental Material [26]. Although the relaxation time of an electron depends on the Fermi energy, we adopted the constant relaxation time approximation for simplicity. To calculate the relaxation time by first-principles calculations, we should consider in the future electron-phonon and phonon-phonon interactions for estimating the relaxation time of an electron and a phonon at the same level of approximation.

Phonon dispersion curves were calculated by the PHONOPY package [36]. The κ_l is evaluated by the phonon lifetime, which is self-consistently calculated in the SHENGBTE package [37]. The second-order harmonic interatomic force constants (IFCs) are calculated within the PHONOPY package, and the third-order anharmonic IFCs are evaluated by using a 3×2×1 supercell and up to the fifth-nearest neighbors considered by SHENGBTE.

III. RESULTS AND DISCUSSIONS

To understand the high thermoelectric performance in β'-SnX, we investigate the structural, thermal, and electronic transport properties of the β'-SnX systems as follows.

A. Structure and stability of β'-SnX

First, we show the results of a global search on 2D structures of tin chalcogenides Sn$_{1-x}X_x$ (X = Te, Se, and S). In Fig. 2, we show the formation enthalpy ΔH [defined in Eq. (1) in the Supplemental Material] of tin chalcogenide 2D systems as a function of chalcogenide composition in the variable-composition convex hulls as predicted by USPEX. In the convex hull, the zero line connects two points at $\Delta H = 0$ for the most stable 2D elementary structures of Sn and chalcogenide as predicted by USPEX. The two most stable structures of Sn-Te as highlighted in blue and red dots in the convex hull

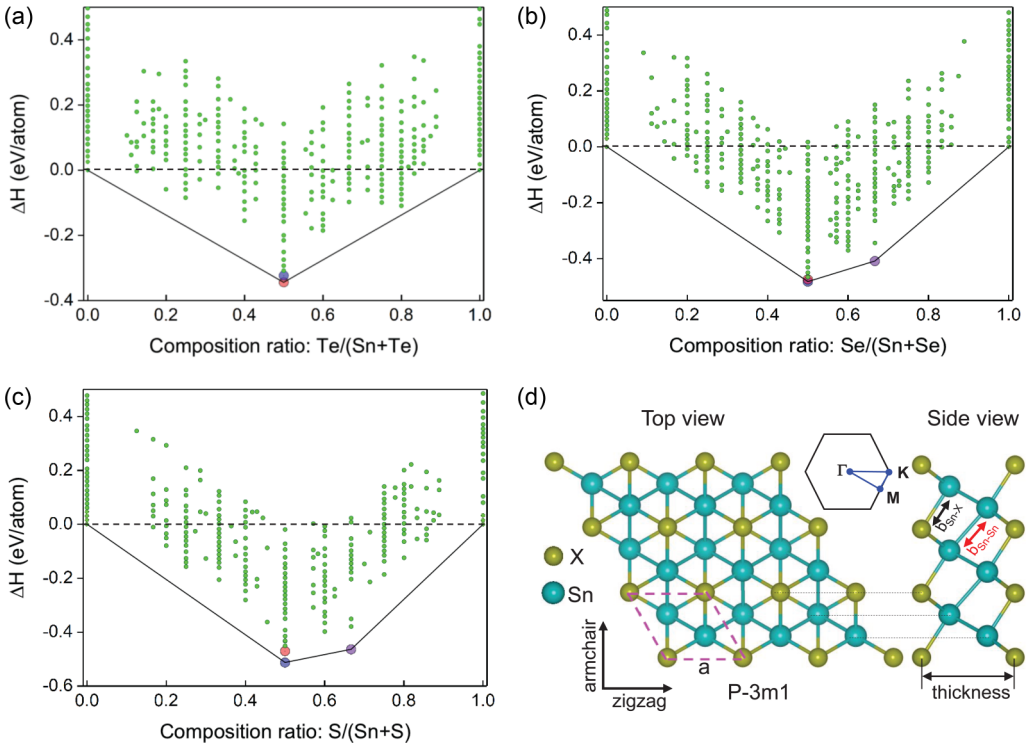

FIG. 2. Convex hull of Sn-X (X = Se, S, and Te) materials searched by USPEX and atomic structure of β'-SnX. USPEX-predicted formation enthalpy ΔH of 2D binary structures with different stoichiometries between (a) Sn and Se, (b) Sn and S, and (c) Sn and Te. The blue and purple dots represent the stable structural phases experimentally observed, and the red dots represent the new β'-phase of SnX. (d) Both top and side views of the atomic structure of β'-SnX, where light-blue and dark-yellow represent Sn and X (X = Te, Se, and S), respectively. The unit cell is marked by the pink dashed lines, and the first Brillouin zone is shown. Armchair, zigzag, and thickness directions are indicated by arrows.

in Fig. 2(a) are the commonly observed puckered orthorhombic SnTe phase [Fig. 1S(a) in the Supplemental Material] [1] and the new β' SnTe phase, respectively. ΔH of the β' SnTe is lower by 19 meV/at than the puckered orthorhombic SnTe phase. The β' SnTe has actually been proposed to be a stable semiconductor by Sa [38] and Zhang *et al.* [39]. Here we substantiate the structural stability of the β' phase in a convex hull with all possible stoichiometries considered.

The β' phase of both Sn-Se and Sn-S has also been obtained close to the convex hulls, as shown by red dots in Figs. 2(b) and 2(c). However, the β' phase is less stable than the puckered orthorhombic phase [13], with ΔH slightly higher by 8 meV/at for SnSe and 42 meV/at for SnS. Additionally, octahedral 1T phases of both $SnSe_2$ and SnS_2, the former of which has been synthesized by experiment [40], are found to be stable (i.e., on the convex hull), as shown by purple dots in Figs. 2(b) and 2(c). In this paper, we will focus only on the β' phases.

All the β' phases have $P\bar{3}m1$ symmetry (space group no. 164), with the optimized atomic structure and lattice parameters of β'-SnX (X = Te, Se, and S) shown in Fig. 2(d) and Table I, respectively. From Fig. 2(d), the β' structure can be viewed as a buckled hexagonal lattice of Sn with two X atoms (one up and one down) at the center of the hexagon. Or as shown in Fig. 1S(b) in the Supplemental Material, it can be considered as two stacked β-SnTe monolayers, one of which takes a series of symmetry operations (inversion + glide) to get the second layer, which makes the β' phase distinct from and more stable than the AB-stacked β-bilayer in which a translation symmetry exists between two β monolayers. The relative stability of the β'-SnTe phase over the AB-stacked β-bilayer is analyzed in more detail in the Supplemental Material [26].

To assess the stability of β'-SnTe, we calculated the phonon dispersion curves of the β' phase of SnX, as shown in Fig. 3(a). No imaginary phonon frequencies are found, showing that β' phases are dynamically stable. Stability was also checked by computing the elastic constants, which were found to indeed satisfy criteria of elastic (mechanical) stability [41–44]. Table I and Supplemental Material [26] give values of the elastic properties of these structures.

B. Thermal transport properties of β'-SnX

Thermoelectric properties consist of thermal and electronic transport properties. We first study the thermal transport properties of β'-SnX. Since thermal transport of a lattice is related to its mechanical properties, let us discuss those properties first. Young's modulus of β'-SnX (less than 50 N/m), as shown in Table I, is much smaller than that of 2D materials such as graphene (∼345 N/m) and phosphorene (∼23–92 N/m) [45]. The shear modulus of β'-SnX is found to be less than 20 N/m. From the phonon dispersion in Fig. 3(a), we can see anticrossing of the phonon dispersion between low-frequency optical vibration modes with acoustic phonon modes for β'-SnX. These optical phonon modes correspond to

TABLE I. Structural and mechanical parameters for the β'-SnX. Here a is the lattice constant, $b_{\text{Sn-Sn}}$ ($b_{\text{Sn-}X}$) are the Sn-Sn and Sn-X bond lengths, and the thickness for 2D SnX is the vertical distance between the two outermost X atoms in Angstroms, as shown in Fig. 1. In-plane Young and shear modules in units of N m^{-1} are listed.

	a (Å)	$b_{\text{Sn-Sn}}$ (Å)	$b_{\text{Sn-}X}$ (Å)	Thickness (Å)	Young's modulus (N m^{-1})	Shear modulus (N m^{-1})	Poisson's ratio
SnTe	4.34	3.36	2.97	5.39	47.15	18.42	0.28
SnSe	4.09	3.37	2.76	5.26	45.77	17.17	0.33
SnS	3.95	3.38	2.64	5.12	45.32	16.53	0.37

twofold-degenerate in-plane shearing modes and the out-of-plane breathing mode. Interestingly, their vibrational frequencies are almost independent of materials at around 50 cm^{-1} at the Γ point, which is closely related to their similar and low values of the shear modulus as given in Table I. In Fig. 3(b), the calculated κ_L is plotted as a function of T for armchair and zigzag directions. For example, κ_L of β'-SnTe at 300 K along the armchair direction is as low as 2.87 W m^{-1} K^{-1}. A typical T dependence of κ_L ($\kappa_L \sim 1/T$) reveals that the umklapp process in the phonon scattering is essential for the temperature range that we studied. In Fig. 3(c), we show the normalized κ_L by cumulative thermal conductivity κ_c as a function of frequency ω at room temperature. κ_c is the value of κ_L when only phonons with mean free paths below a threshold are considered [37]. Over 90% of the κ_L is contributed by phonon modes with frequency below 80 cm^{-1} for SnTe, in which the three acoustic modes and the three low-frequency optical modes contribute to κ_L.

The low lattice thermal conductivity of β'-SnX arises not only from low elastic constants due to weak Sn-Sn bonding strength, but also from strong lattice anharmonicity. In the low-frequency region, Fig. S3(a) in the Supplemental Material shows that anharmonic scattering dominates the phonon-phonon interactions (PPIs), as seen by comparing the anharmonic three-phonon scattering rates (ASRs) and isotopic scattering rates (ISRs). These ASRs are mainly contributed by the phonon absorption process (ASRs+). Among the three β'-SnX's, the strongest ASRs are found in SnS, which corresponds to the lowest κ_L. It is worth noting that the highest value of ASRs is located between around 50 and 100 cm^{-1}, where acoustic and three low-frequency optical modes are mixed together. Thus we expect that the interband scattering between the acoustic and optical modes is associated with the large ASRs.

C. Thermoelectric properties of β'-SnX

Based on the calculated results, we will discuss the thermoelectric properties of β'-SnX.

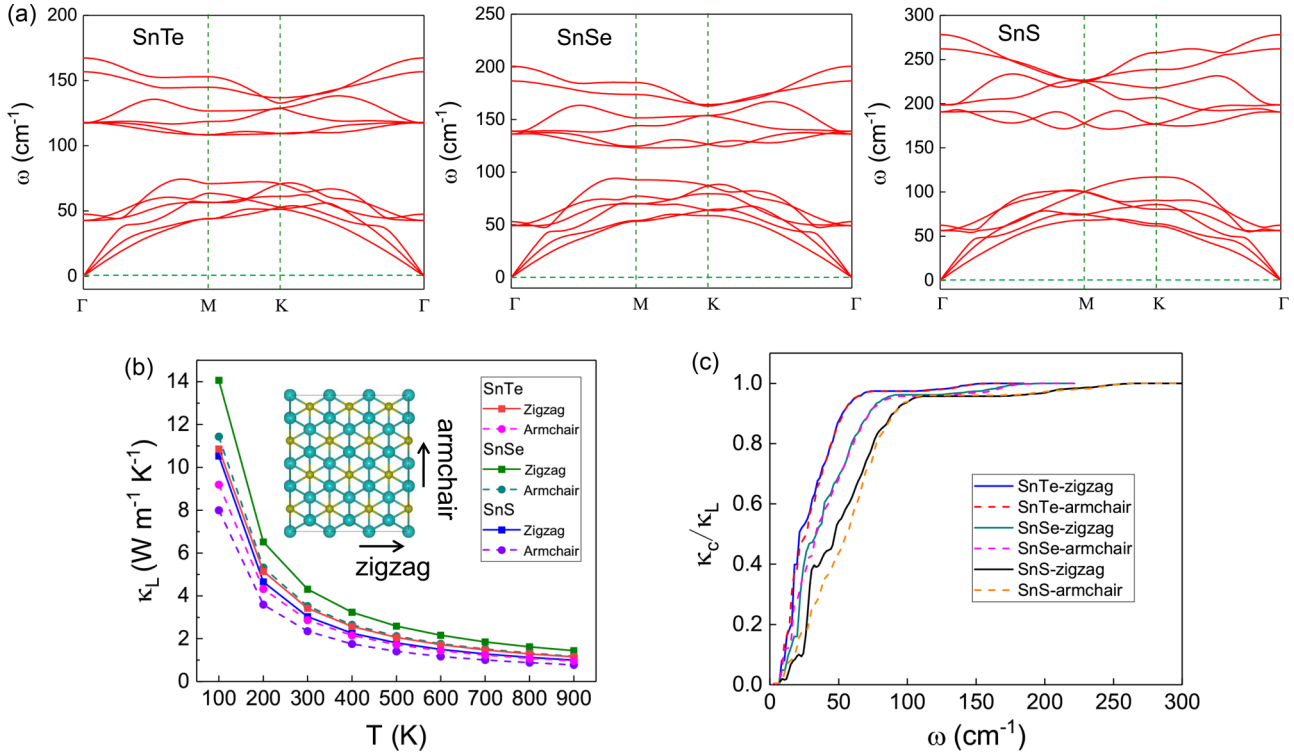

FIG. 3. Lattice thermal properties of β'-SnX. (a) Phonon-dispersion relation, (b) lattice thermal conductivity κ_L, and (c) normalized cumulative thermal conductivity κ_c/κ_L as a function of phonon frequency.

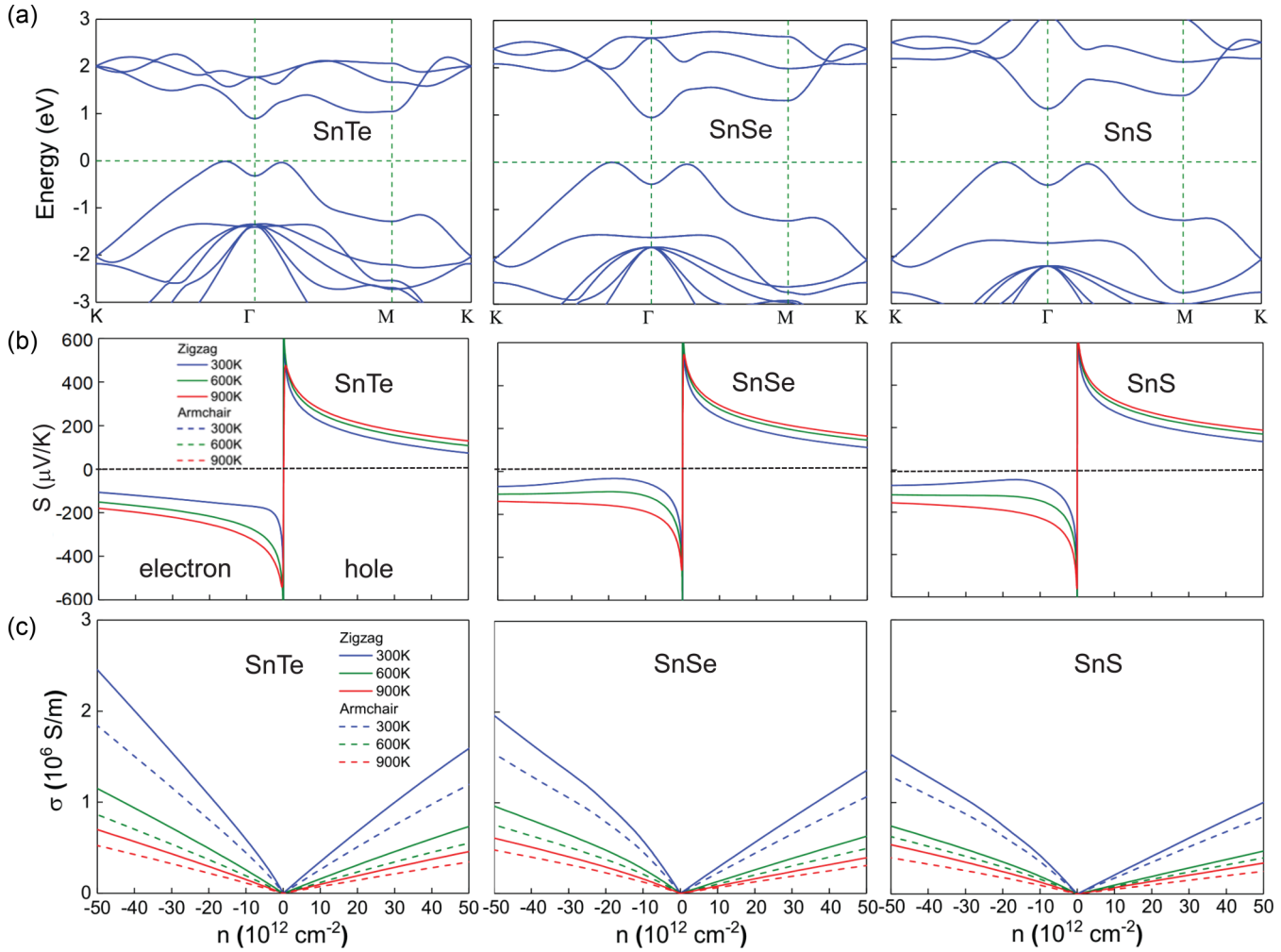

FIG. 4. Electrical transport properties of β'-SnX. (a) Electronic band structure, (b) Seebeck coefficients S, and (c) electrical conductivity σ of SnX for zigzag and armchair directions, as a function of carrier density for $T = 300$, 600, and 900 K.

1. Seebeck coefficient

The calculated structural stability and low thermal conductivity suggest that β'-SnX can be considered suitable for thermoelectric applications. To unveil its potential for energy conversion between heat and electricity, we look into the relevant electronic band structure and electrical properties, both of which reinforce its capacity for such an application. In Fig. 4(a), we show electronic band structures of β'-SnX's. Indirect band gaps of β'-SnX's exist near the zone center. The value of the energy gaps is around 1.0 eV, which is independent of chalcogenide atoms. It is noted that the conduction bands have been upshifted to fit the band gap obtained by hybrid functional calculations [46], which usually give a more reliable band-gap size. According to the $E_g \sim 10 k_B T_{\text{opt}}$ rule [47], the optimal working temperature for thermoelectric applications of such materials should be around 1000 K.

Thermoelectric properties are closely related to electronic band structure. For all β'-SnX's, we found the following features in the electronic bands: (i) Band dispersions of the valence-band maximum (VBM) and the conduction-band minimum (CBM) along both ΓK and ΓM directions are quite similar, which corresponds to a similar effective mass along both the zigzag and armchair directions as given in Table II. According to Cutler *et al.* [48] and Snyder *et al.* [49], for a parabolic band within the energy-independent scattering approximation, the Seebeck coefficient takes the form of $S = \frac{8\pi^2 k_B^2 m^* T}{3eh^2}(\frac{\pi}{3n})^{2/3}$, where m^* is the effective mass of the carrier and n is the carrier concentration. From this formula, similar to the effective mass m^*, one expects no directional dependence of the Seebeck coefficient, as shown in Fig. 4(b), in which dashed lines practically coincide with solid lines. (ii) A usual quadratic dispersion relation appears for the carriers at the CBM, while a quartic band dispersion ($E_k \sim k^4$) is found at the VBM, which usually brings about flat bands near the Fermi level. Thus a constant electronic density of states (DOS) appears near the CBM, while a van-Hove DOS singularity divergence appears near the VBM [50], as shown in Fig. 4S in the Supplemental Material. Such a difference of DOS between the VBM and CBM explains why the effective mass of holes is larger than that of electrons, as is shown in Table II.

In Figs. 4(b) and 4(c), we show Seebeck coefficient and electrical conductivity. For β'-SnSe and β'-SnS, the Seebeck coefficient of hole carriers is larger than that of an electron, while the electrical conductivity σ of a hole is smaller than

TABLE II. Carrier mobility at 300 K and effective mass for SnX. The effective mass is in units of electron mass m_0 (9.11×10^{-32} kg). The method in the Supplemental Material gives more details on calculating carrier mobility μ [26].

		SnTe		SnSe		SnS	
		hole	electron	hole	electron	hole	electron
Carrier mobility μ	zigzag	1364	1112	1275	853	1220	764
($cm^2\,V^{-1}\,s^{-1}$)	armchair	576	834	579	694	468	660
Effective mass m^*	zigzag	0.213	0.144	0.228	0.169	0.363	0.218
(m_0)	armchair	0.227	0.144	0.228	0.163	0.363	0.212

that of an electron, which is expected for a parabolic band within an energy-independent scattering approximation [49]. However, an opposite trend is found in β'-SnTe that the Seebeck coefficient of an electron is higher than that of a hole, which is due to the convergence of the conduction band minimum at the Γ point with a flat band edge at the M point. This type of band convergence is quite advantageous for an enhancement of the Seebeck coefficient [51].

2. Electrical conductivity

In Fig. 4(c), we plot the calculated electrical conductivity σ as a function of carrier concentration n for zigzag and armchair directions. Decent electrical conductivity σ as high as a few 10^6 S/m at room temperature is obtained for the three β'-SnX's. Differences of σ for different materials along different directions can be understood from the carrier mobility μ and the effective mass m^*, as is shown in Table II. From Table II, we can point out that (i) the effective mass m^* depends not on crystal direction but on carrier type, for example $m_h^* > m_e^*$; (ii) carrier mobility μ along the zigzag direction is larger than that along the armchair direction, due to a smaller deformation potential along the zigzag direction than the armchair direction. All these features lead to a preference of the zigzag over the armchair direction and an electron over a hole carrier for optimal electrical conductivity σ, which is indicated by the comparison between solid (zigzag) and dashed (armchair) lines as is shown in Fig. 4(c). Moreover, σ decreases with increasing temperature, which is associated with the intrinsic phonon scattering mechanism. The electrical thermal conductivity κ_e is also calculated based on the Boltzmann transport theory, as given in Fig. 5S of the Supplemental Material, and it fits the Wiedemann-Franz law in combination with σ.

3. Power factor and figure of merit

With the Seebeck coefficient, electrical conductivity, and thermal conductivity available, we finally evaluate the power factor (PF) and the dimensionless figure of merit (ZT). In Figs. 5(a) and 5(b), we plot the dependence of carrier type, crystalline direction, and temperature for PF and ZT. The optimal PF and ZT are shown in Figs. 5(c) and 5(d). As is seen from Fig. 5(a), PF remains as high as 0.01 $W\,K^{-2}\,m^{-1}$ or above in a wide range of temperatures at a carrier concentration from 10^{12} to 10^{13} cm^{-2}. Because of the high PF and relatively low κ, it is no surprise to observe a quite promising value of ZT in β'-SnX. From Fig. 5(b), all ZT of β'-SnX appear above 1.0 at 900 K in the doping range of interest ($|n| < 8\times10^{13}$ cm^{-2}). ZT of β'-SnTe can even go above 2.0 at 600 K, which makes the material very competitive against the present commercialized thermoelectric materials. From Figs. 5(a) and 5(b), both PF and ZT are larger for a hole than for an electron in β'-SnS and β'-SnSe, mainly due to the smaller Seebeck coefficient of an electron than a hole. As for β'-SnTe, we get a better thermoelectric performance of an electron than a hole, which is due to a large S and PF from the concept of "band convergence" [51,52] at the CBM concurrent with decent electrical conductivity from the smaller effective mass of an electron than that of a hole. In Ref. [51], the dependence of optimal PF^{opt} on ΔE for a generic system with band convergence is given quantitatively within the two-band model, with ΔE defined as valley splitting energy. PF^{opt} decreases exponentially with increasing ΔE within a few k_BT. In our case, ΔE is the energy difference of the CBMs between the K and M points in Fig. 4(a), and ΔE is 0.15, 0.36, and 0.28 eV for β' SnTe, SnSe, and SnS, respectively, which explains why a much bigger PF^{opt} of the n-type β' SnTe is obtained than that of the n-type β' SnSe and SnS.

In Figs. 5(c) and 5(d), we show the optimal values of PF and ZT for two types of carriers along the armchair and zigzag directions at $T = 300$, 600, and 900 K. It is more clear to see in Figs. 5(a) and 5(b) that n-type β'-SnTe has a much better thermoelectric performance than β'-SnS and β'-SnSe, while p-type β'-SnX shows a very decent performance but no obvious difference of PF and ZT from SnS to SnTe.

It should be pointed out that we expect some discrepancy between theoretical and experimental values. For our estimation, the discrepancy is due to the following reasons: (i) the constant relaxation time approximation was used for electronic transport properties, where the real relaxation time may vary with the carrier concentration; (ii) only isotopic and three-phonon scattering were considered here for κ_L. The constant relaxation time approximation may overestimate σ. However, κ_L may also be overestimated without considering scattering from the impurities, vacancies, interstitials, dislocations, grain boundaries, and so on. Considering that the two parameters κ_L and σ are both overestimated, the deviation of TE performance may be mitigated in part by the two effects. Therefore, our estimated TE performance may give a reasonable agreement with the experimental values.

Finally, due to the confinement effect for a 2D system [7,8], it is important to evaluate the PF enhancement factor f_E [9], which is defined as $f_E = (\frac{L}{\Lambda})^{D-3}$, where L is the spatial confinement length, Λ ($= \sqrt{\frac{2\pi\hbar^2}{k_BTm^*}}$) is the so-called thermal de Broglie wavelength, and D ($= 1$ or 2) is the dimensionality.

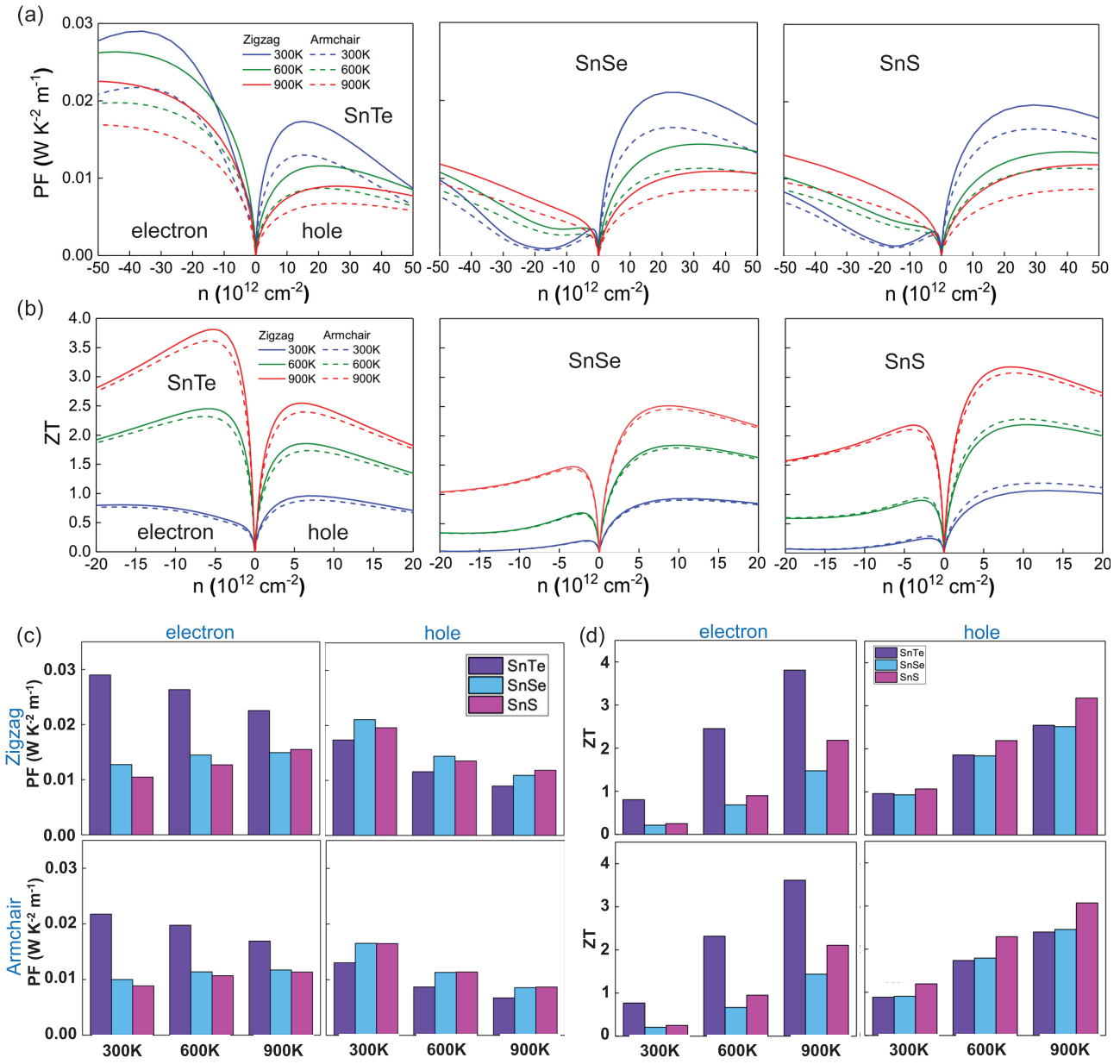

FIG. 5. Thermoelectric performance for β'-SnX. (a,c) Power factor (PF) and (b), (d) figure of merit ZT of SnX as a function of doping level n at different temperatures. Here n is the electron (negative) or hole (positive) doping per unit surface area for 2D SnX. Blue, green, and red represent 300, 600, and 900 K, and solid and dashed lines represents the zigzag and armchair directions, respectively, which are shown in Fig. 2. The maximum PF and ZT at optimum doping level as a function of temperature and crystal direction are shown in (c) and (d).

Here we consider the PF enhancement from 3D to 2D. L is taken from the interlayer distance in 3D counterparts. Values of Λ, L, and F_E for β'-SnX are given in Table III in the Supplemental Material. Taking n-type β'-SnTe as an example, we find that $\Lambda \sim 11.35$ nm and $L \sim 0.82$ nm, which makes $f_E \sim 13.76$, about one order of magnitude from 3D to 2D, revealing that the thermoelectric behavior of β'-SnX in 2D form is much enhanced compared with its 3D counterpart.

In summary, for the new β' phase of SnX, remarkable thermoelectric properties exceed those of traditional thermoelectric materials because of the following reasons: (i) the low-dimensional structure with high elastic and dynamic stability, which shows substantial enhancement of the power factor relative to the bulk phase due to the larger thermal de Broglie length Λ; (ii) low shear modulus within the layer, giving rise to an ultralow frequency of the shearing mode, which can couple very effectively with the acoustic phonon mode to greatly suppress lattice thermal conductivity; and (iii) convergence of electronic bands at the valence- and conduction-band edges. All the above factors appear concurrently and coherently to lead to the good thermoelectric performance.

IV. CONCLUSION

In this paper, we found new-phase SnX (β' phase), which is suitable for thermoelectric application by combining the

ab initio density-functional theory with evolutionary algorithm USPEX and semiclassical Boltzmann transport theory. The β' phase is either the most stable phase (β'-SnTe) or close to the most stable phases (such as the orthorhombic phase of SnSe and SnS) that are experimentally observed. Calculations of phonon dispersion curves and of the elastic constants were used to confirm structural stability. Low lattice thermal conductivity is obtained for β'-SnX, mainly because of hybridization of acoustic phonon modes with low-frequency interlayer shearing vibration modes. High values of the power factor ($\sim$0.01 $\mathrm{W\,m^{-1}\,K^{-2}}$) are also observed in our calculations, and it is ascribed to band convergence at the CBM and quartic electronic band dispersion at the VBM. Remarkable values of the dimensionless figure of merit can be obtainable in β'-SnX within practical doping of a few $10^{12}\mathrm{cm}^{-2}$. In particular, ZT over 2.5 can be reached in β'-SnTe at 900 K. Thermoelectric performance of β'-SnX can be further optimized with transport along the zigzag crystalline direction. Our theoretical study may facilitate the discovery of a new phase for optimizing thermoelectric performance by experiment.

ACKNOWLEDGMENTS

This work is supported by the National Key R&D Program of China (2017YFA0206301) and the Major Program of Aerospace Advanced Manufacturing Technology Research Foundation NSFC and CASC, China (No. U1537204). A.R.O. and B.J.D. thank the Russian Science Foundation (Grant No. 16-13-10459). R.S. acknowledges JSPS KAKENHI Grants No. JP25107005, No. JP25286005, No. JP15K21722, and No. JP18H01810. N.T.H. acknowledges JSPS KAKENHI Grant No. JP18J10151. Z.H.W. thanks the National Science Foundation of China (Grant No. 11604159). Calculations were performed on XSEDE facilities and on the cluster of the Center for Functional Nanomaterials, Brookhaven National Laboratory, which is supported by the DOE-BES under Contract No. DE-AC02-98CH10086. This work has been carried out using the Rurik supercomputer, the Arkuda supercomputer of Skolkovo Foundation, and computing resources of the federal collective usage center Complex for Simulation and Data Processing for Mega-science Facilities at NRC Kurchatov Institute.

[1] K. Chang, J. Liu, H. Lin, N. Wang, K. Zhao, A. Zhang, F. Jin, Y. Zhong, X. Hu, W. Duan, Q. Zhang, L. Fu, Q.-K. Xue, X. Chen, and S.-H. Ji, Science **353**, 274 (2016).

[2] Y. Tanaka, Z. Ren, T. Sato, K. Nakayama, S. Souma, T. Takahashi, K. Segawa, and Y. Ando, Nat. Phys. **8**, 800 (2012).

[3] L.-D. Zhao, S.-H. Lo, Y. Zhang, H. Sun, G. Tan, C. Uher, C. Wolverton, V. P. Dravid, and M. G. Kanatzidis, Nature (London) **508**, 373 (2014).

[4] J. P. Heremans, V. Jovovic, E. S. Toberer, A. Saramat, K. Kurosaki, A. Charoenphakdee, S. Yamanaka, and G. J. Snyder, Science **321**, 554 (2008).

[5] C. W. Li, J. Hong, A. F. May, D. Bansal, S. Chi, T. Hong, G. Ehlers, and O. Delaire, Nat. Phys. **11**, 1063 (2015).

[6] S. Lee, K. Esfarjani, T. Luo, J. Zhou, Z. Tian, and G. Chen, Nat. Commun. **5**, 3525 (2014).

[7] L. D. Hicks and M. S. Dresselhaus, Phys. Rev. B **47**, 16631 (1993).

[8] L. D. Hicks and M. S. Dresselhaus, Phys. Rev. B **47**, 12727 (1993).

[9] N. T. Hung, E. H. H. Hasdeo, A. R. T. Nugraha, M. S. Dresselhaus, and R. Saito, Phys. Rev. Lett. **117**, 036602 (2016).

[10] K. S. Novoselov, A. K. Geim, S. V. Morozov, D. Jiang, Y. Zhang, S. V. Dubonos, I. V. Grigorieva, and A. A. Firsov, Science **306**, 666 (2004).

[11] K. F. Mak, C. Lee, J. Hone, J. Shan, and T. F. Heinz, Phys. Rev. Lett. **105**, 136805 (2010).

[12] H. Liu, A. T. Neal, Z. Zhu, Z. Luo, X. Xu, D. Tomanek, and P. D. Ye, ACS Nano **8**, 4033 (2014).

[13] L. Li, Z. Chen, Y. Hu, X. Wang, T. Zhang, W. Chen, and Q. Wang, J. Am. Chem. Soc. **135**, 1213 (2013).

[14] R. Fei, A. Faghaninia, R. Soklaski, J.-A. Yan, C. Lo, and L. Yang, Nano Lett. **14**, 6393 (2014).

[15] A. Shafique and Y.-H. Shin, Sci. Rep. **7**, 506 (2017).

[16] J. Shen, Z. Ma, and K. Wu, Sci. Rep. **7**, 8914 (2017).

[17] Z. Y. Al Balushi, K. Wang, R. K. Ghosh, R. A. Vila, S. M. Eichfeld, J. D. Caldwell, X. Qin, Y.-C. Lin, P. A. DeSario, G. Stone, S. Subramanian, D. F. Paul, R. M. Wallace, S. Datta, J. M. Redwing, and J. A. Robinson, Nat. Mater. **15**, 1166 (2016).

[18] B. Aufray, A. Kara, S. Vizzini, H. Oughaddou, C. Léandri, B. Ealet, and G. Le Lay, Appl. Phys. Lett. **96**, 183102 (2010).

[19] A. R. Oganov, A. O. Lyakhov, and M. Valle, Acc. Chem. Res. **44**, 227 (2011).

[20] A. O. Lyakhov, A. R. Oganov, H. T. Stokes, and Q. Zhu, Comput. Phys. Commun. **184**, 1172 (2013).

[21] A. R. Oganov, Y. Ma, A. O. Lyakhov, M. Valle, and C. Gatti, Rev. Mineral. Geochem. **71**, 271 (2010).

[22] A. O. Lyakhov, A. R. Oganov, and M. Valle, Crystal structure prediction using evolutionary approach, in *Modern Methods of Crystal Structure Prediction* (Wiley-VCH, Weinheim, 2010), Chap. 7, pp. 147–180.

[23] G. Kresse and J. Furthmüller, Phys. Rev. B **54**, 11169 (1996).

[24] G. Kresse and D. Joubert, Phys. Rev. B **59**, 1758 (1999).

[25] J. P. Perdew, K. Burke, and M. Ernzerhof, Phys. Rev. Lett. **77**, 3865 (1996).

[26] See Supplemental Material at http://link.aps.org/supplemental/10.1103/PhysRevMaterials.3.013405 for more details on the parameters of the method, structure description and discussions on structural stability.

[27] G. K. Madsen and D. J. Singh, Comput. Phys. Commun. **175**, 67 (2006).

[28] J. Bardeen and W. Shockley, Phys. Rev. **80**, 72 (1950).

[29] J. Qiao, X. Kong, Z.-X. Hu, F. Yang, and W. Ji, Nat. Commun. **5**, 4475 (2014).

[30] Y. Cai, G. Zhang, and Y.-W. Zhang, J. Am. Chem. Soc. **136**, 6269 (2014).

[31] Z. Jin, Q. Liao, H. Fang, Z. Liu, W. Liu, Z. Ding, T. Luo, and N. Yang, Sci. Rep. **5**, 18342 (2015).

[32] L.-C. Zhang, G. Qin, W.-Z. Fang, H.-J. Cui, Q.-R. Zheng, Q.-B. Yan, and G. Su, Sci. Rep. **6**, 19830 (2016).

[33] H. Y. Lv, W. J. Lu, D. F. Shao, H. Y. Lu, and Y. P. Sun, J. Mater. Chem. C **4**, 4538 (2016).
[34] A. Shafique, A. Samad, and Y.-H. Shin, Phys. Chem. Chem. Phys. **19**, 20677 (2017).
[35] P. Jiang, H. Liu, L. Cheng, D. Fan, J. Zhang, J. Wei, J. Liang, and J. Shi, Carbon **113**, 108 (2017).
[36] A. Togo and I. Tanaka, Scr. Mater. **108**, 1 (2015).
[37] W. Li, J. Carrete, N. A. Katcho, and N. Mingo, Comput. Phys. Commun. **185**, 1747 (2014).
[38] B. Sa, Z. Sun, and B. Wu, Nanoscale **8**, 1169 (2016).
[39] X. Zhang, Z. Yang, and Y. Chen, J. Appl. Phys. **122**, 064101 (2017).
[40] Z. Xing, G. Lin, T. Wenming, Z. Qi, J. Shengye, L. Huiqiao, B. Yoshio, G. Dmitri, and Z. Tianyou, Adv. Mater. **27**, 8035 (2015).
[41] F. Mouhat and F.-X. Coudert, Phys. Rev. B **90**, 224104 (2014).
[42] M. Born, Math. Proc. Cambridge Philos. Soc. **36**, 160 (1940).
[43] J. Zhou and R. Huang, J. Mech. Phys. Solids **56**, 1609 (2008).
[44] J. Wang, R. Zhang, D.-H. Ding, and R. Wang, Acta Cryst. Sec. A **55**, 558 (1999).
[45] L. Kou, C. Chen, and S. C. Smith, J. Phys. Chem. Lett. **6**, 2794 (2015).
[46] A. V. Krukau, O. A. Vydrov, A. F. Izmaylov, and G. E. Scuseria, J. Chem. Phys. **125**, 224106 (2006).
[47] H. Ehrenreich and F. Spaepen, *Solid State Physics* (Academic Press, San Diego, 1998), Vol. 51.
[48] M. Cutler, J. F. Leavy, and R. L. Fitzpatrick, Phys. Rev. **133**, A1143 (1964).
[49] G. J. Snyder and E. S. Toberer, Nat. Mater. **7**, 105 (2018).
[50] L. Seixas, A. S. Rodin, A. Carvalho, and A. H. Castro Neto, Phys. Rev. Lett. **116**, 206803 (2016).
[51] N. T. Hung, A. R. T. Nugraha, T. Yang, Z. Zhang, and R. Saito, J. Appl. Phys. **125**, 082502 (2019).
[52] Y. Pei, X. Shi, A. LaLonde, H. Wang, L. Chen, and G. J. Snyder, Nature (London) **473**, 66 (2011).